

## Original Article

## Deep learning-enabled MRI-only photon and proton therapy treatment planning for paediatric abdominal tumours



Mateusz C. Florkow<sup>a,\*</sup>, Filipa Guerreiro<sup>b,\*</sup>, Frank Zijlstra<sup>a</sup>, Enrica Seravalli<sup>b</sup>, Geert O. Janssens<sup>c,d</sup>, John H. Maduro<sup>e</sup>, Antje C. Knopf<sup>e</sup>, René M. Castelein<sup>f</sup>, Marijn van Stralen<sup>a,g</sup>, Bas W. Raaymakers<sup>b</sup>, Peter R. Seevinck<sup>a,g</sup>

<sup>a</sup> Image Sciences Institute; <sup>b</sup> Department of Radiotherapy; <sup>c</sup> Department of Radiation Oncology, University Medical Centre Utrecht; <sup>d</sup> Princess Máxima Centre for Paediatric Oncology, Utrecht; <sup>e</sup> Department of Radiation Oncology, University Medical Centre Groningen, University of Groningen; <sup>f</sup> Department of Orthopaedics, University Medical Centre Utrecht; and <sup>g</sup> MRIguidance B.V., Utrecht, The Netherlands

## ARTICLE INFO

## Article history:

Received 18 May 2020

Received in revised form 24 September 2020

Accepted 28 September 2020

Available online 7 October 2020

## Keywords:

Synthetic CT

Deep learning

Paediatric

MRI

Wilms' Tumour

Neuroblastoma

## ABSTRACT

**Purpose:** To assess the feasibility of magnetic resonance imaging (MRI)-only treatment planning for photon and proton radiotherapy in children with abdominal tumours.

**Materials and methods:** The study was conducted on 66 paediatric patients with Wilms' tumour or neuroblastoma (age  $4 \pm 2$  years) who underwent MR and computed tomography (CT) acquisition on the same day as part of the clinical protocol. MRI intensities were converted to CT Hounsfield units (HU) by means of a UNet-like neural network trained to generate synthetic CT (sCT) from T1- and T2-weighted MR images. The CT-to-sCT image similarity was evaluated by computing the mean error (ME), mean absolute error (MAE), peak signal-to-noise ratio (PSNR) and Dice similarity coefficient (DSC). Synthetic CT dosimetric accuracy was verified against CT-based dose distributions for volumetric-modulated arc therapy (VMAT) and intensity-modulated pencil-beam scanning (PBS). Relative dose differences ( $D_{\text{diff}}$ ) in the internal target volume and organs-at-risk were computed and a three-dimensional gamma analysis (2 mm, 2%) was performed.

**Results:** The average  $\pm$  standard deviation ME was  $-5 \pm 12$  HU, MAE was  $57 \pm 12$  HU, PSNR was  $30.3 \pm 1.6$  dB and DSC was  $76 \pm 8\%$  for bones and  $92 \pm 9\%$  for lungs. Average  $D_{\text{diff}}$  were  $<0.5\%$  for both VMAT (range  $[-2.5; 2.4]\%$ ) and PBS (range  $[-2.7; 3.7]\%$ ) dose distributions. The average gamma pass-rates were  $>99\%$  (range  $[85; 100]\%$ ) for VMAT and  $>96\%$  (range  $[87; 100]\%$ ) for PBS.

**Conclusion:** The deep learning-based model generated accurate sCT from planning T1w- and T2w-MR images. Most dosimetric differences were within clinically acceptable criteria for photon and proton radiotherapy, demonstrating the feasibility of an MRI-only workflow for paediatric patients with abdominal tumours.

© 2020 The Authors. Published by Elsevier B.V. Radiotherapy and Oncology 153 (2020) 220–227 This is an open access article under the CC BY license (<http://creativecommons.org/licenses/by/4.0/>).

Wilms' tumour (WT) and neuroblastoma (NBL) are two of the most common abdominal solid tumours diagnosed in children. Depending on the risk stratification, the treatment involves a combination of surgery, chemotherapy and radiotherapy [1,2]. During

radiotherapy treatment planning (RTP), magnetic resonance imaging (MRI) scans are commonly acquired to define the target volume thanks to their superior soft tissue contrast [3]. In addition, computed tomography (CT) images are used for the computation of patient-specific dose deposition maps [4] using the conversion of the CT Hounsfield units (HU) to relative electron density for photon therapy or to stopping power ratio relative to water for proton therapy.

In the last decade, MRI-only workflows have been developed using MRI-based synthetic CT (sCT) images to calculate the dose deposition [5–7]. Such workflows are especially useful for anatomies in which MRI-CT registration for contour propagation is difficult [8]. By omitting the CT acquisition, systematic uncertain-

\* Corresponding authors at: University Medical Center Utrecht, 3508 GA Utrecht, The Netherlands.

E-mail addresses: [m.c.florkow@umcutrecht.nl](mailto:m.c.florkow@umcutrecht.nl) (M.C. Florkow), [f.guerreiro@umcutrecht.nl](mailto:f.guerreiro@umcutrecht.nl) (F. Guerreiro), [f.zijlstra-2@umcutrecht.nl](mailto:f.zijlstra-2@umcutrecht.nl) (F. Zijlstra), [e.seravalli@umcutrecht.nl](mailto:e.seravalli@umcutrecht.nl) (E. Seravalli), [g.o.r.janssens@umcutrecht.nl](mailto:g.o.r.janssens@umcutrecht.nl) (G.O. Janssens), [j.h.maduro@umcg.nl](mailto:j.h.maduro@umcg.nl) (J.H. Maduro), [a.c.knopf@umcg.nl](mailto:a.c.knopf@umcg.nl) (A.C. Knopf), [r.m.castelein@umcutrecht.nl](mailto:r.m.castelein@umcutrecht.nl) (R.M. Castelein), [m.vanstralen-2@umcutrecht.nl](mailto:m.vanstralen-2@umcutrecht.nl) (M. van Stralen), [b.w.raaymakers@umcutrecht.nl](mailto:b.w.raaymakers@umcutrecht.nl) (B.W. Raaymakers), [p.seevinck@umcutrecht.nl](mailto:p.seevinck@umcutrecht.nl) (P.R. Seevinck).

<sup>1</sup> Authors contributed equally to this work.

ties arising from the MRI-CT registration are eliminated and logistics are simplified in the treatment preparation phase.

In the last few years, the use of sCT has been reported for RTP of the brain [9], head and neck [10], lungs [11], prostate [12,13] and abdomen [14,15] in adult patients. Specifically in the abdomen, sCT images have been investigated for the treatment of liver tumours using photon [14] and proton [15] therapies. For the paediatric population, studies reporting sCT generation methods are scarce [16,17], with only one approach generating sCT in children with abdominal tumours [16]. Paediatric patients are certainly challenging because of their substantial inter-patient morphological variability. Nevertheless, they would potentially benefit the most from the simplified MRI-only workflows, with a reduced time under anaesthesia during treatment preparation.

In this study, we investigated the feasibility of an MRI-only treatment planning workflow for children with abdominal tumours using an end-to-end deep learning approach to generate sCT from planning T1- and T2-weighted MR images. Dose calculations on the sCT images were compared against CT-based dose distributions for volumetric-modulated arc therapy (VMAT) and intensity-modulated pencil beam scanning (PBS).

## Materials and methods

This retrospective study was performed in accordance with the institutional review board (WAG/mb/17/008865).

### Data collection

Images of 66 children, treated for WT ( $n = 24$ ) or NBL ( $n = 42$ ) at the Radiotherapy Department of the University Medical Centre Utrecht (UMCU) between April 2015 and July 2020, were collected for this study. Patients had a mean age ( $\pm$  standard deviation (SD)) of  $4 \pm 2$  years old (range: [1; 9] years) at the time of scanning and the female-to-male ratio was 28/38.

For treatment preparation, patients underwent four-dimensional (4D)-CT and MR scanning less than an hour apart. During the image acquisition, 54/66 patients were under general anaesthesia and all patients were fixated in supine position in an individualized vacuum mattress (Bluebag, Elekta, Stockholm, Sweden) with the arms wide along the body.

### Acquisition parameters

The 4D-CT images were acquired by means of a respiratory belt (Philips Bellow System, Philips Medical System, Best, The Netherlands) from a 16-, 40-, or 64-channel detector scanner (Brilliance, Philips Medical Systems, Best, The Netherlands) with an in-plane isotropic resolution ranging from 0.8 to 1.2 mm and a slice spacing between 2 and 3 mm. The tube voltage varied between 90 and 120 kV and the tube current between 30 and 250 mA. The 4D-CT was acquired in ten phases which were averaged to obtain the planning-CT as per our institution clinical practice.

The MRI acquisition, performed on a 1.5T scanner (Achieva, Philips Medical Systems, Best, The Netherlands), included a T1-weighted (T1w) 3D gradient-echo sequence and a T2-weighted (T2w) 3D turbo spin echo sequence. T1w-MR images were obtained in the axial plane at a resolution of  $0.7 \times 0.7 \times 1.5 \text{ mm}^3$ . The echo/repetition times were 2.7 ms/5.4 ms with a flip angle of  $10^\circ$ . T2w-MR images were acquired in the coronal plane at a resolution of  $0.8 \times 0.8 \times 1.1 \text{ mm}^3$ . The echo/repetition times were 90 ms/454 ms with a flip angle of  $90^\circ$ . Respiratory motion artefacts were reduced during MR scanning using the phase encoding artefact reduction (PEAR) method. Both MRI acquisitions were part of the clinical protocol and were not optimized for sCT generation.

### Data processing

#### Pre-processing

MR images were independently and non-rigidly registered to the planning-CT using the Elastix toolbox [18] in order to get the best voxelwise match between modalities. The registration was a composition of a translation, an Euler transform and a cubic B-spline, optimized using mutual information and regularized with a rigidity penalty [19]. During registration, MR images were resampled to the planning-CT resolution using a cubic B-spline interpolation.

For the sCT generation only, MR and planning-CT images were normalized independently and per volume. MR intensities were clipped beyond the 95th percentile and the resulting intensities were linearly mapped to  $[-1; 1]$ . CT intensities were linearly mapped from  $[-1024; 3071]$  to  $[-1; 1]$ .

#### Synthetic CT generation

The proposed end-to-end deep learning sCT generation approach is an extension of a previously reported model [20], which used a neural network derived from a U-Net [21]. The network used 3D patches from the registered T1w- and T2w-MR images as inputs to generate sCT patches of the same resolution as the planning-CT images.

The network was trained simultaneously on both T1w- and T2w-MR images since it proved superior to models trained only on T1w- or T2w-images (Supplementary material Table 1). Thus, the model presented in [20] was slightly modified to first process the T1w- and T2w-MR images separately with two convolution layers. The information extracted from the two images was concatenated before starting the standard encoding path of the U-Net, as described in Fig. 1.

During the training phase, the generated sCT images were compared to the planning-CT using a L1 loss (absolute voxelwise difference). The resulting error was minimized using a Nadam [22] optimizer, given a learning rate of  $10^{-4}$ . The training was stopped after 100,000 iterations. The remaining parameters were the same as in [20]. Synthetic CT images were generated in two phases. First, a 3-fold cross-validation (CV) was performed on 54 patients with 18 patients set aside for testing in each fold. Then a model was trained on the 54 patients of the CV set and evaluated on a fully independent test set consisting of 12 patients.

### Treatment planning

For both WT and NBL patients, the clinical target and organs-at-risk (OARs) delineated by a radiation oncologist were used in this study. The gross tumour volume (GTV) consisted of the pre-operative tumour extension, including pathologic lymph nodes and residual disease if applicable. The clinical target volume was created by expanding the GTV by 5 mm for NBL patients and by 10 mm for WT patients. To account for the respiratory motion, an internal target volume (ITV) was delineated for each patient by using the minimum and maximum 4D-CT phases and surgical clips as motion surrogates [23]. OARs included the kidneys (divided into ipsilateral and contralateral kidneys), the liver and the spleen.

RTP was performed in RayStation (RaySearch Laboratories, Stockholm, Sweden) for both VMAT and PBS dose distributions. In accordance with the clinical protocol at the UMCU, VMAT plans consisted of a 6MV full-arc. PBS plans were optimized for the purpose of this study using 2–3 posterior-oblique irradiation fields to exploit the dorsal location of the target. The number and direction of the proton beams (range  $[120^\circ; 240^\circ]$ ) were patient-specific. The prescribed dose ranged from 10.8 to 36 Gy and was delivered in 6

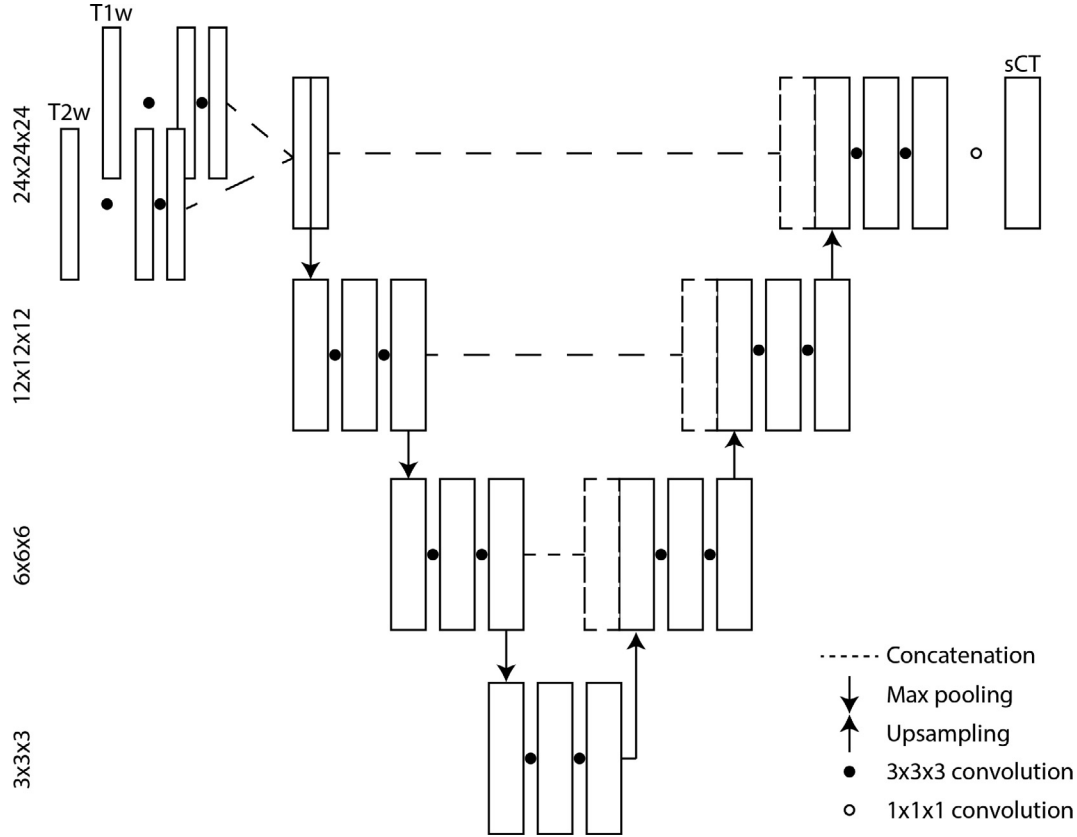


**Fig. 1.** Architecture of the U-Net. T1-weighted (T1w) and T2-weighted (T2w) MR patches of size  $24 \times 24 \times 24$  were input to the neural network separately. After two convolutions, patches were concatenated to undergo the standard encoding–decoding process of the U-Net. Encoding was performed using max pooling and decoding with nearest neighbour upsampling. The resulting sCT image has the same resolution as the planning-CT. The spatial dimension of each level is given on the left hand side.

to 20 fractions, depending on the histology and the presence of residual disease.

3D plan optimization was performed using the planning-CT, a uniform 3 mm dose grid, a collapse cone engine for VMAT and a pencil-beam algorithm for intensity-modulated PBS dose distributions. To ensure a fair dosimetric comparison, both dose distributions were ITV-based robustly optimized and evaluated accounting for a 5 mm patient set-up uncertainty and a 3% range uncertainty (only for PBS). In addition, a relative biological effectiveness of 1.1 was included during planning for PBS.

VMAT and PBS plans were optimized using a minimax optimization method [24] whilst its robustness was evaluated using a minimum evaluation dose map ( $V_{wmin}$ ) [25]. Plans were considered robust if, in the  $V_{wmin}$ , 98% of the ITV received at least 95% of the prescribed dose [25]. In addition, to reduce the risk of asymmetric skeletal growth, a homogeneous dose avoiding left–right dose gradients higher than 5 Gy was aimed for the primary ossification centres of the vertebra volume adjacent to the ITV [26].

## Evaluation

### • Technical evaluation

Synthetic CT images were compared against the planning-CT using distance and structural metrics. The distance metrics consisted of voxelwise differences between the HU of the planning-CT and of the sCT, within the body contour, the soft tissue, the bone and the lungs. In particular, mean error (ME) was computed to estimate any systematic bias in the sCT generation and mean absolute error (MAE) to estimate the overall error.

Structural metrics included Dice similarity coefficient (DSC) [27] and peak-signal-to-noise ratio (PSNR). DSC measured the overlap of bone and lungs between the planning-CT and sCT images. PSNR measured the reconstruction quality and was computed as:

$$PSNR = 10 \log_{10} \left( \frac{4095^2}{1/N \sum_{i=1}^N (I_{CT}(i) - I_{sCT}(i))^2} \right)$$

All metrics were computed only in regions where T1w-, T2w-MR and CT information was available. Regions where  $HU > 200$  were labelled as bone and regions where  $-200 < HU < 200$  were labelled as soft tissue. Lungs were segmented independently on the planning-CT and sCT images using a dedicated in-house clinical tool [28].

### • Dosimetric evaluation

To evaluate the dosimetric acceptability of sCT, CT-based VMAT and PBS dose distributions were re-calculated on the sCT images.

Planning-CT and sCT dose differences were compared using dose-volume histogram (DVH) metrics and 3D global gamma analysis [29]. DVH metrics included  $D_{98\%}$ ,  $D_{50\%}$ ,  $D_{2\%}$  and  $V_{95\%}$  for the ITV as well as mean dose ( $D_{mean}$ ) and  $D_{2\%}$  for the OARs. CT–sCT DVH dose differences in the target and OARs smaller than 2% at a 95% confidence interval were considered clinically acceptable, as proposed by Korsholm et al. [30]. 3D global gamma pass-rates were computed using the CT dose as reference, multiple dose thresholds (10%, 50%, 90%), a 2 mm distance to agreement and a 2% dose difference (2 mm, 2%). Gamma pass-rates were calculated within a body mask excluding the arms to neglect CT–MR mismatch in this

region (eg. registration errors, arms not in the field of view of one image). In addition, the correlation between the DVH and gamma results and the use of anaesthesia during image acquisition was verified using a two-tailed student's *t*-test at a 0.05 significance level.

## Results

For an example patient with a MR matrix of size 429x429x149, sCT images were generated under 200 s on a GeForce GTX 1080 Ti (NVIDIA, California, USA) graphics processing unit.

Table 1 summarizes the average ME, MAE, DSC and PSNR obtained separately for both CV and test set patients and across the entire population. Notably, no differences were found in terms of technical performance between the CV and test patients with metrics within the same range in both sets. Most errors occurred

in the bone with HU largely underestimated on the sCT images, as indicated by the high ME. Large errors were also found in the lungs, despite a high overlap of their bulk structure between CT and sCT.

Fig. 2, which compares planning-CT and sCT images for two patients, shows that voxelwise differences were partially caused by inter-scan differences. This includes differences originating from patient positioning during image acquisition (i.e skin outline, clavicle position), breathing motion (i.e volume and internal structures of the lungs and ribs) and physiological changes (i.e bowel filling) that were not corrected by the registration.

Relative dose differences of clinically relevant DVH parameters between the planning-CT and sCT dose distributions are shown in the box-and-whisker plots in Fig. 3(a) for the ITV and in Fig. 3(b),(c) for the OARs. Similarly to the technical performance, no differences were found between the CV and test patients results with DVH metrics within the same range in both sets.

**Table 1**

Average  $\pm$  standard deviation (SD) of the mean error (ME), mean absolute error (MAE), Dice similarity coefficient (DSC) and peak signal-to-noise ratio (PSNR) computed between the planning-CT and sCT across the cross-validation (CV) set, the test set and the entire population.

Metric	Body site	Average (±SD [Range])				
		CV (n = 54)		Test (n = 12)	Overall (n = 66)	
ME (HU)	Body	−5 ± 11	[−30; 42]	−7 ± 13	[−22; 15]	−5 ± 12
	Soft tissue	0 ± 8	[−17; 27]	1 ± 12	[−10; 35]	0 ± 9
	Bone	114 ± 59	[−12; 307]	132 ± 35	[66; 178]	117 ± 55
	Lungs	−9 ± 61	[−155; 146]	−5 ± 77	[−200; 90]	−9 ± 67
MAE (HU)	Body	56 ± 11	[35; 86]	62 ± 13	[39; 86]	57 ± 12
	Soft tissue	33 ± 6	[22; 55]	36 ± 8	[26; 53]	33 ± 7
	Bone	156 ± 43	[79; 322]	167 ± 22	[118; 198]	158 ± 40
	Lungs	105 ± 33	[50; 212]	104 ± 38	[66; 215]	105 ± 34
DSC (%)	Bone	76 ± 7	[50; 87]	76 ± 6	[65; 83]	76 ± 8
	Lungs	92 ± 9	[45; 99]	88 ± 7	[71; 94]	92 ± 9
PSNR (dB)	Body	30.4 ± 1.6	[26.7; 33.7]	30.0 ± 1.8	[27.7; 34.3]	30.3 ± 1.6

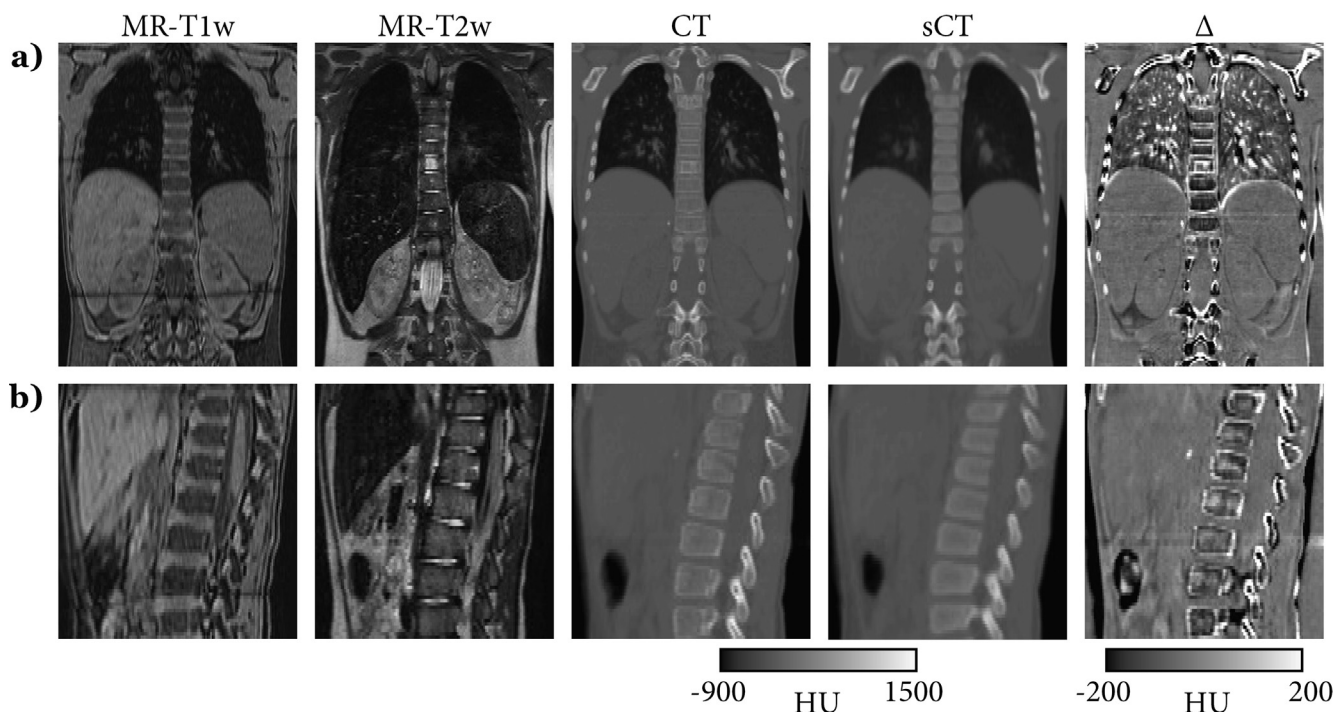


**Fig. 2.** T1-weighted MR, T2-weighted MR, planning-CT and sCT images in the sagittal and coronal planes for two example patients from the cross-validation set (a) and from the independent test set (b). The error map ( $\Delta$  [CT-sCT]) on the right shows the difference in Hounsfield units (HU) between the planning-CT and sCT images.

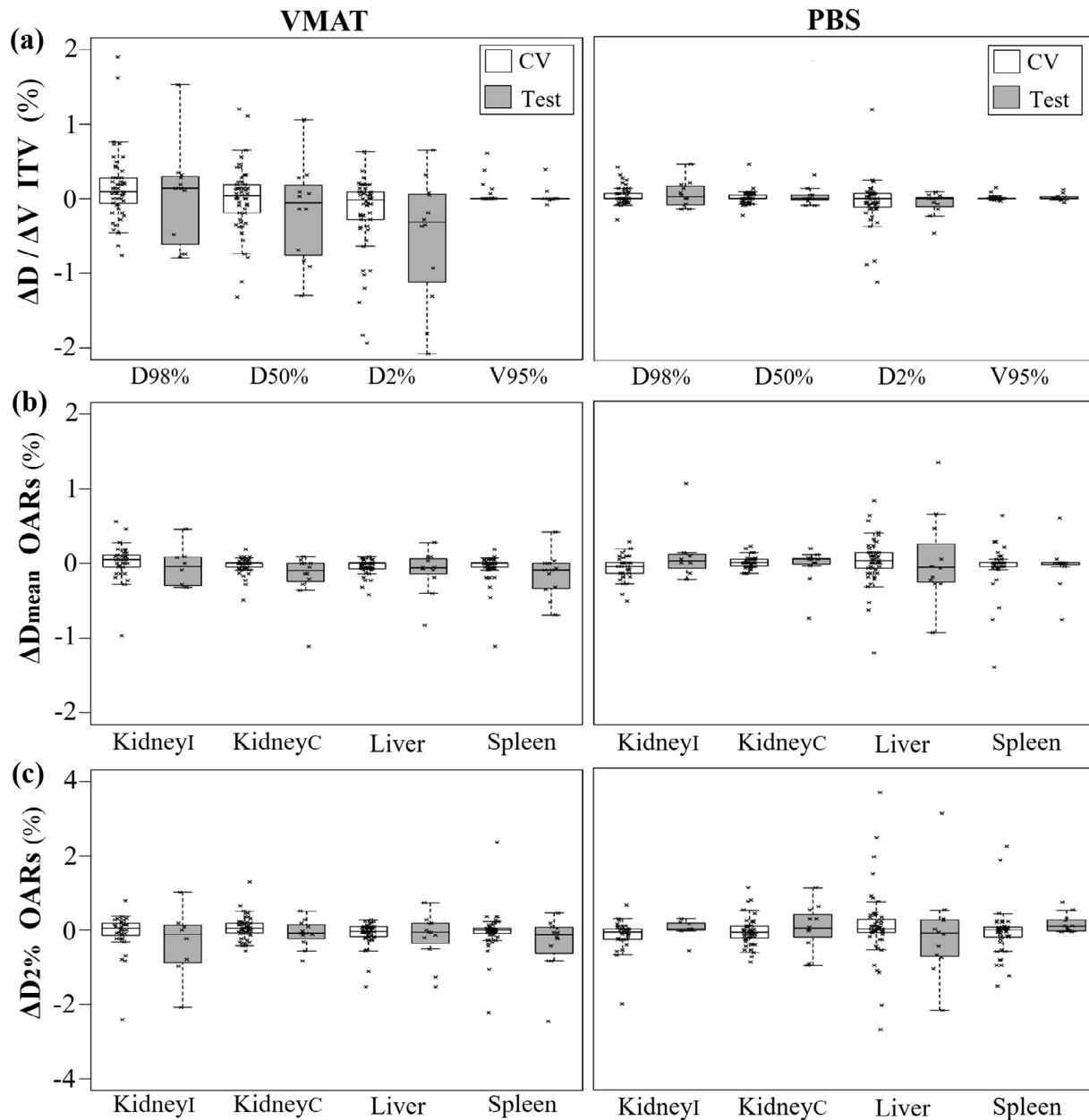


**Fig. 3.** Box-and-whisker plots of the dose-volume histogram (DVH) parameters relative differences between the planning-CT, used as reference, and the sCT dose distributions for VMAT (left) and PBS (right) for patients from the cross-validation (CV) (in white) and test (in grey) sets. (a) ITV DVH parameters differences (b) Mean dose ( $D_{\text{mean}}$ ) differences for the OARs (c)  $D_{2\%}$  differences for the OARs. Crosses indicate differences per patient. Values are presented as a percentage of the respective prescribed dose. Abbreviations: Kidney<sub>I</sub> = ipsilateral kidney; Kidney<sub>C</sub> = contralateral kidney.

For the ITV, DVH parameters differed on average by less than 0.5% (range [−2.1; 1.9]%) for VMAT and by less than 0.1% (range [−1.1; 1.2]%) for PBS dose distributions for all patients (Fig. 3(a)). For the OARs, average DVH differences were under 0.3% for both VMAT and PBS dose distributions (Fig. 3(b),(c)).  $D_{\text{mean}}$  differences ranged from [−1.1; 0.6] for VMAT and [−1.4; 1.3] for PBS. Similarly,  $D_{2\%}$  differences ranged from [−2.5; 2.4] for VMAT and [−2.7; 3.7] for PBS.

Fig. 4 shows relative dose difference maps for three example patients. For the VMAT dose distributions, larger dosimetric differences were seen due to (1) changes in the position of air cavities between the body outline and the ITV (Fig. 4(b),(c)) and (2) changes in the CT-sCT body outline (Fig. 4(c)). For the PBS dose

distributions, because posterior irradiation fields were used, CT to sCT dose differences were predominantly resulting from a different positioning of air cavities in the vicinity of the ITV (Fig. 4(b),(c)).

Gamma pass-rates (2%, 2 mm) obtained between the planning-CT and sCT dose distributions are given in Table 2. Average gamma pass-rates were above 99% for VMAT and above 96% for PBS dose distributions. Individual gamma pass-rates were lower than 90% for 2 patients on the VMAT and for 3 patients on the PBS dose distributions (example patients in Fig. 4(b),(c)).

In addition, no significant statistical differences were found in the dosimetric DVH and gamma results between patients imaged with and without anaesthesia ( $p > 0.05$ ).



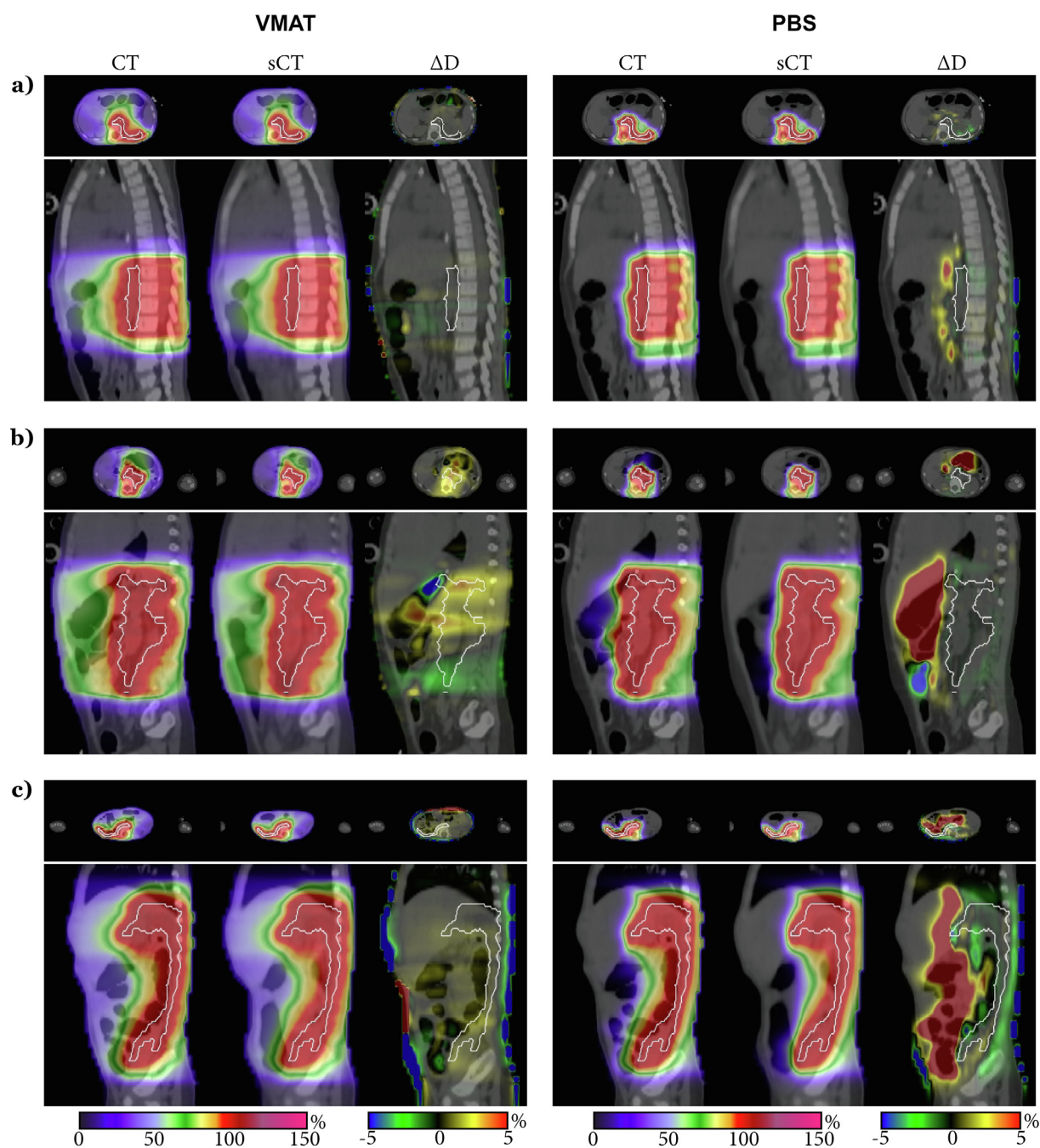


**Fig. 4.** Dose maps optimized on the planning-CT and re-calculated on the sCT images for VMAT and PBS dose distributions for three example patients from the cross-validation (a, b) and independent test (c) sets. The last column displays the dose difference maps (CT-sCT) overlaid on the planning-CT image. The scale is expressed as a percentage of the prescribed dose (21.6 Gy for (a, b) and 10.8 Gy for (c)). Patients in (b) and (c) had gamma pass-rates below 90% as a result of (1) CT-sCT different air cavities distributions and (2) CT-sCT body outline differences.

## Discussion

In this study, the feasibility of a deep learning-based sCT generation method for photon and proton treatment planning in paediatric patients with abdominal tumours was evaluated. We presented an end-to-end method to generate sCT from planning T1w- and T2w-MR images. We found clinically acceptable differences between the planning-CT and sCT dose distributions for both photon and proton therapy on this morphologically heterogeneous dataset. To the authors' knowledge, the present study is the first evaluating the feasibility of performing dose calculations on

deep-learning based sCT for children younger than 10 years old with abdominal tumours.

Facing the low number of patients treated per year and the ethical adversities within the children population to acquire imaging data, datasets including both CT and MR images in treatment position for over 60 patients in a single institute are rare. To thoroughly exploit the entire population, technical and dosimetric evaluation of the sCT images were performed on both a CV and a fully independent test sets. No differences were found between the CV and test sets in terms of technical and dosimetric results, confirming the generalization performance of the proposed network.

**Table 2**

Average  $\pm$  standard deviation [range] gamma pass-rates using a 2% and 2 mm criterion with multiple dose thresholds (10%, 50%, 90%) for VMAT and PBS dose distributions optimized on the planning-CT and re-calculated on the sCT across the cross-validation (CV) set, the test set and the entire population.

Threshold	VMAT (%)			PBS (%)		
	CV (n = 54)	Test (n = 12)	Overall	CV (n = 54)	Test (n = 12)	Overall
10%	99.7 $\pm$ 0.5 [96.2; 100]	99.7 $\pm$ 0.3 [99.2; 100]	99.7 $\pm$ 0.5	97.4 $\pm$ 2.9 [87.5; 100]	96.2 $\pm$ 4.0 [86.8; 100]	97.2 $\pm$ 3.1
50%	99.7 $\pm$ 1.0 [94.1; 100]	99.8 $\pm$ 0.5 [98.4; 100]	99.7 $\pm$ 0.9	99.4 $\pm$ 1.1 [94.8; 100]	98.6 $\pm$ 2.0 [94.4; 100]	99.2 $\pm$ 1.3
90%	99.5 $\pm$ 2.4 [85.4; 100]	99.5 $\pm$ 1.5 [94.9; 100]	99.5 $\pm$ 2.3	99.6 $\pm$ 1.1 [93.6; 100]	99.2 $\pm$ 1.1 [97.2; 100]	99.5 $\pm$ 1.1

The technical accuracy of the sCT generated in this study, with average MAE<sub>body</sub> of 57 HU, MAE<sub>soft tissue</sub> of 33 HU, MAE<sub>bone</sub> of 158 HU and MAE<sub>lungs</sub> of 105 HU, compared favourably with literature. A study in adult patients with hepatic cancer [15] reported a MAE<sub>body</sub> of 73  $\pm$  18 HU, a MAE<sub>bone</sub> of 217  $\pm$  63 HU and a MAE<sub>soft tissue</sub> of 59  $\pm$  31 HU. A previous study, performed on a subset of this dataset [16], obtained a MAE<sub>bone</sub> of 212  $\pm$  40 HU, a MAE<sub>soft tissue</sub> of 53  $\pm$  7 HU and a MAE<sub>lungs</sub> of 125  $\pm$  24 HU using a combined atlas- and voxel-based method. Although performed on similar anatomies, these two studies had different MRI-to-CT registration techniques, using rigid [16] or non-rigid [15] registration, which make them difficult to compare. In the present study, we made the choice to non-rigidly register the planning-CT and MR images aiming for an optimal voxelwise match between modalities while minimizing distortions with a rigidity penalty. Therefore, dose differences related to registration errors were minimized to focus on the HU differences between CT and sCT. Note that for a prospective clinical use of the model, only a standard rigid registration between the T1w- and T2w-MR images would be required. Despite the non-rigid registration, registration errors were still observed, especially for the body outline and for the bones and lungs, which resulted in blurring [31].

The dosimetric accuracy of the generated sCT was evaluated for both VMAT and PBS dose distributions optimized using the planning-CT. Clinically acceptable dose differences ( $\leq 2\%$ ) were obtained for all patients on the ITV and for 61/66 patients on the OARs for both VMAT and PBS. Differences larger than 2% were only obtained for the D<sub>2%</sub> points. Nevertheless, these D<sub>2%</sub> dose differences are not clinically significant since the tolerance doses for these OARs are far from being reached using the clinical prescribed doses. For the ITV, larger differences between the planning-CT and sCT doses were detected for the VMAT dose distributions due to bowel filling variations and body outline differences between images (Fig. 4). A potential reduction of these differences could be expected if a posterior partial arc and/or air density override during optimization of the VMAT dose distributions were used. For PBS, results showed that when using posterior-oblique irradiation fields, the differences between planning-CT and sCT dose distributions on the ITV were minimized (Fig. 4). For the OARs, larger dosimetric differences were observed for both VMAT and PBS dose distributions especially for the liver and spleen as a result of their location in the vicinity of the lungs. At soft tissue-to-air interfaces (i.e. lungs, skin), higher HU variations can arise due to misalignments introduced by motion or registration errors between the planning-CT and MR images. Concerning the skin outline, previous studies [16,32,33] have applied the skin outline extracted from the planning-CT on the sCT to correct for these misalignments and lower the CT-to-sCT dose difference. In this study, the planning-CT outline information was not used for the dose re-calculation on the sCT images. Thus, the present CT-sCT skin outline misalignment might have led to an overestimation of the observed dosimetric differences.

In terms of gamma pass-rates, both VMAT and PBS showed clinically acceptable results with average gamma pass-rates over 96% for a (2%, 2 mm) criterion. Photon gamma pass-rates with a (2%,

2 mm) criterion and a 10% dose threshold obtained in this study (99.7  $\pm$  0.5%) compared favourably with the literature, reporting pass-rates of 97.7  $\pm$  2.2% for the same patient category [16]. Similarly, proton gamma pass-rates in this study (97.2  $\pm$  3.1%) were in agreement with values reported in literature with pass-rates of 97.0  $\pm$  2.9% for liver cancer treatment [15] and of 87.1  $\pm$  5.4% for the same patient category [16]. Nevertheless, for a reduced number of patients, gamma pass-rates were below 90% for both VMAT (n = 2) and PBS (n = 3) potentially due to (1) target size and location (i.e. at the lungs interface) and (2) inter-scan differences (i.e. body outline, bowel filling). Because of these inter-scan differences, which would not be present in a clinical setting, the dosimetric differences showed in this study might be interpreted as an overestimation of the real difference between the planning-CT and sCT.

Overall, the results of this study demonstrated that MRI-only photon and proton dose calculations on the generated sCT images were clinically feasible, even when using MR images not optimized for the sCT generation. The deep learning methodology used to generate sCT enabled the creation of a model which coped with the morphological variability of the paediatric population. With an application in the abdominal region, in which MRI-CT registration is particularly hard, this method is promising for radiotherapy treatment planning and would ease the clinical workflow for paediatric population whilst potentially improving its accuracy.

## Funding

Support of NVIDIA Corporation with the donation of GPU for this research.

This work is part of the research program Applied and Engineering Sciences (TTW) with project number 15479 which is (partly) financed by the Netherlands Organization for Scientific Research (NWO).

## Declaration of Competing Interest

The authors declare the following financial interests/personal relationships which may be considered as potential competing interests: M. van Stralen and P.R. Seevinck are minority shareholders at MRIguidance B.V.

## Appendix A. Supplementary data

Supplementary data to this article can be found online at <https://doi.org/10.1016/j.radonc.2020.09.056>.

## References

- [1] Van Den Heuvel-Eibrink MM, Hol JA, Pritchard-Jones K, Van Tinteren H, Furtwängler R, Verschuur AC, et al. Position Paper: Rationale for the treatment of Wilms tumour in the UMBRELLA SIOP-RTSG 2016 protocol. *Nat Rev Urol* 2017;14:743–52. <https://doi.org/10.1038/nrurol.2017.163>.
- [2] Ladenstein R, Pötschger U, Pearson ADJ, Brock P, Luksch R, Castel V, et al. Busulfan and melphalan versus carboplatin, etoposide, and melphalan as high-dose chemotherapy for high-risk neuroblastoma (HR-NBL1/SIOPEN): an

- international, randomised, multi-arm, open-label, phase 3 trial. *Lancet Oncol* 2017;18:500–14. [https://doi.org/10.1016/S1470-2045\(17\)30070-0](https://doi.org/10.1016/S1470-2045(17)30070-0).
- [3] Lagendijk JJW, Raaymakers BW, Van Den Berg CAT, Moerland MA, Philippens ME, Van Vulpen M. MR guidance in radiotherapy. *Phys Med Biol* 2014;59: R349–69. <https://doi.org/10.1088/0031-9155/59/21/R349>.
  - [4] Chernak ES, Rodriguez-Antunez A, Jelden GL, Dhaliwal RS, Lavik PS. The use of computed tomography for radiation therapy treatment planning. *Radiology* 1975;117:613–4. <https://doi.org/10.1148/117.3.613>.
  - [5] Edmund JM, Nyholm T. A review of substitute CT generation for MRI-only radiation therapy. *Radiat Oncol* 2017;12:28. <https://doi.org/10.1186/s13014-016-0747-y>.
  - [6] Tenhunen M, Korhonen J, Kapanen M, Seppälä T, Koivula L, Collan J, et al. MRI-only based radiation therapy of prostate cancer: workflow and early clinical experience. *Acta Oncol (Madr)* 2018;57:902–7. <https://doi.org/10.1080/0284186X.2018.1445284>.
  - [7] Hoffmann A, Oborn B, Moteabbed M, Yan S, Bortfeld T, Knopf A, et al. MR-guided proton therapy: a review and a preview. *Radiat Oncol* 2020;15:129. <https://doi.org/10.1186/s13014-020-01571-x>.
  - [8] Jonsson J, Nyholm T, Söderkvist K. The rationale for MR-only treatment planning for external radiotherapy. *Clin Transl Radiat Oncol* 2019;18:60–5. <https://doi.org/10.1016/j.ctro.2019.03.005>.
  - [9] Kazemifar S, McGuire S, Timmerman R, Wardak Z, Nguyen D, Park Y, et al. MRI-only brain radiotherapy: assessing the dosimetric accuracy of synthetic CT images generated using a deep learning approach. *Radiation Oncol* 2019;136:56–63. <https://doi.org/10.1016/j.radonc.2019.03.026>.
  - [10] Dinkla AM, Florkow MC, Maspero M, Savenije MHF, Zijlstra F, Doornaert PAH, et al. Dosimetric evaluation of synthetic CT for head and neck radiotherapy generated by a patch-based three-dimensional convolutional neural network. *Med Phys* 2019. <https://doi.org/10.1002/mp.13663>.
  - [11] Hsu SH, Peng Q, Tomé WA. On the generation of synthetic CT for a MRI-only radiation therapy workflow for the abdomen. *J. Phys. Conf. Ser.*, vol. 1154, Institute of Physics Publishing; 2019. <https://doi.org/10.1088/1742-6596/1154/1/012011>.
  - [12] Depauw N, Keyriläinen J, Suilamo S, Warner L, Bzdusek K, Olsen C, et al. MRI-based IMPT planning for prostate cancer. *Radiation Oncol* 2020;144:79–85. <https://doi.org/10.1016/j.radonc.2019.10.010>.
  - [13] Maspero M, Savenije MHF, Dinkla AM, Seevinck PR, Intven MPW, Jurgenliemk-Schulz IM, et al. Dose evaluation of fast synthetic-CT generation using a generative adversarial network for general pelvis MR-only radiotherapy. *Phys Med Biol* 2018;63. <https://doi.org/10.1088/1361-6560/aada6d>.
  - [14] Bredfeldt JS, Liu L, Feng M, Cao Y, Balter JM. Synthetic CT for MRI-based liver stereotactic body radiotherapy treatment planning. *Phys Med Biol* 2017;62:2922–34. <https://doi.org/10.1088/1361-6560/aa5059>.
  - [15] Liu Y, Lei Y, Wang Y, Wang T, Ren L, Lin L, et al. MRI-based treatment planning for proton radiotherapy: Dosimetric validation of a deep learning-based liver synthetic CT generation method. *Phys Med Biol* 2019;64. <https://doi.org/10.1088/1361-6560/ab25bc>.
  - [16] Guerreiro F, Koivula L, Seravalli E, Janssens GO, Maduro JH, Brouwer CL, et al. Feasibility of MRI-only photon and proton dose calculations for pediatric patients with abdominal tumors. *Phys Med Biol* 2019;64. <https://doi.org/10.1088/1361-6560/ab0095>.
  - [17] Ladefoged CN, Marner L, Hindsholm A, Law I, Højgaard L, Andersen FL. Deep learning based attenuation correction of PET/MRI in pediatric brain tumor patients: evaluation in a clinical setting. *Front Neurosci* 2019;13. <https://doi.org/10.3389/fnins.2018.01005>.
  - [18] Klein S, Staring M, Murphy K, Viergever MA, Pluim JPW. Elastix: A toolbox for intensity-based medical image registration. *IEEE Trans Med Imaging* 2010;29:196–205. <https://doi.org/10.1109/TMI.2009.2035616>.
  - [19] Staring M, Klein S, Pluim JPW. A rigidity penalty term for nonrigid registration: a rigidity penalty term for nonrigid registration. *Med Phys* 2007;34:4098–108.
  - [20] Florkow MC, Zijlstra F, Willemsen K, Maspero M, Berg CAT, Kerkmeijer LGW, et al. Deep learning-based MR-to-CT synthesis: The influence of varying gradient echo-based MR images as input channels. *Magn Reson Med* 2019. <https://doi.org/10.1002/mrm.28008>.
  - [21] Ronneberger O, Fischer P, Brox T. U-net: Convolutional networks for biomedical image segmentation. In: Navab N, and Hornegger J, and Wells WM, and Frangi AF, editors. *Lect. Notes Comput. Sci.*, vol. 9351, Cham: Springer International Publishing; 2015, p. 234–41. [https://doi.org/10.1007/978-3-319-24574-4\\_28](https://doi.org/10.1007/978-3-319-24574-4_28).
  - [22] Dozat T. Incorporating Nesterov Momentum into Adam. *ICLR Work* 2016:2013–6.
  - [23] Guerreiro F, Seravalli E, Janssens GO, van de Ven CP, van den Heuvel-Eibrink MM, Raaymakers BW. Intra- and inter-fraction uncertainties during IGRT for Wilms' tumor. *Acta Oncol (Madr)* 2018;57:941–9. <https://doi.org/10.1080/0284186X.2018.1438655>.
  - [24] Fredriksson A, Forsgren A, Hårdemark B. Minimax optimization for handling range and setup uncertainties in proton therapy. *Med Phys* 2011;38:1672–84. <https://doi.org/10.1118/1.3556559>.
  - [25] Korevaar EW, Habraken SJM, Scandurra D, Kierkels RGJ, Unipan M, Eenink MGC, et al. Practical robustness evaluation in radiotherapy – a photon and proton-proof alternative to PTV-based plan evaluation. *Radiation Oncol* 2019;141:267–74. <https://doi.org/10.1016/j.radonc.2019.08.005>.
  - [26] Hoeben BA, Carrie C, Timmermann B, Mandeville HC, Gandola L, Dieckmann K, et al. Management of vertebral radiotherapy dose in paediatric patients with cancer: consensus recommendations from the SIOPE radiotherapy working group. *Lancet Oncol* 2019;20:e155–66. [https://doi.org/10.1016/S1470-2045\(19\)30034-8](https://doi.org/10.1016/S1470-2045(19)30034-8).
  - [27] Dice LR. Measures of the amount of ecologic association between species. *Ecology* 1945;26:297–302. <https://doi.org/10.2307/1932409>.
  - [28] Bol GH, Kotte ANTJ, van der Heide UA, Lagendijk JJW. Simultaneous multi-modality ROI delineation in clinical practice. *Comput Methods Programs Biomed* 2009;96:133–40. <https://doi.org/10.1016/j.cmpb.2009.04.008>.
  - [29] Low DA. Gamma dose distribution evaluation tool. *J Phys: Conf Ser* 2010;250:012071. <https://doi.org/10.1088/1742-6596/250/1/012071>.
  - [30] Korsholm ME, Waring LW, Edmund JM. A criterion for the reliable use of MRI-only radiotherapy. *Radiat Oncol* 2014;9. <https://doi.org/10.1186/1748-717X-9-16>.
  - [31] Florkow MC, Zijlstra F, Kerkmeijer LGW, Maspero M, van den Berg CAT, van Stralen M, et al. The impact of MRI-CT registration errors on deep learning-based synthetic CT generation. In: Angelini ED, Landman BA, editors. *Med. Imaging 2019 Image Process.*, vol. 10949, SPIE; 2019, p. 116. <https://doi.org/10.1117/12.2512747>.
  - [32] Maspero M, van den Berg CAT, Landry G, Belka C, Parodi K, Seevinck PR, et al. Feasibility of MR-only proton dose calculations for prostate cancer radiotherapy using a commercial pseudo-CT generation method. *Phys Med Biol* 2017;62:9159–76. <https://doi.org/10.1088/1361-6560/aa9677>.
  - [33] Koivula L, Wee L, Korhonen J. Feasibility of MRI-only treatment planning for proton therapy in brain and prostate cancers: dose calculation accuracy in substitute CT images: Feasibility of MRI-only treatment planning for proton therapy. *Med Phys* 2016;43:4634–42. <https://doi.org/10.1118/1.4958677>.